Internship Report

Frequency dependent squeezing in current ground based gravitational wave detectors

Tangchao Liu

M2 International Centre for Fundamental Physics
Theoretical Physics

Supervisors: Eleonora Capocasa, Matteo Barsuglia

tangchao.liu@universite-paris-saclay.fr

Astroparticule et Cosmologie

June 2023

Abstract

Quantum noise in ground based gravitational wave detectors arises from the vacuum fluctuation coming from the output port of the interferometer. Replacing this vacuum by a squeezed one turns out to be capable of reducing the quantum noise. The originally used frequency independent squeezing can only improve the sensitivity at high frequencies, since the error ellipse is squeezed and rotated by the response of the interferometer. Hence frequency dependent squeezing (FDS) by the use of filter cavity (FC) is desired to counteract this ponderomotive squeezing in order to achieve a quantum noise reduction over all frequency range. For the current dual recycled interferometers, one FC is enough to achieve the optimal FDS in the Resonant Sideband Extraction (RSE) regime. For the VIRGO detector the possibility of detuned RSE (DRSE) has been considered because of higher order laser modes generated due to the marginally stable recycling cavity. This work is devoted to the optimization of FDS for VIRGO in the DRSE regime, by optimizing over the FC detuning frequency, initial squeezing angle and FC input mirror transmissivity (which determines the FC bandwidth) of the single FC configuration currently available in VIRGO. Specifically the quadrature input-output relation and quantum noise spectral density for Michleson interferometer are derived and the same formulae for dual recycled interferometer are also given. An analytic formula is obtained for optimal squeezing with one FC in the RSE regime. After this reproduction of well established results in the literature, numerical simulation is done to find the optimal performance of current VIRGO detector with one FC in terms of binary neutron star (BNS) range, by use of the Matlab code `gwinc` developed by the community. Starting from a baseline of BNS range of 87.9 Mpc, changing only the FC detuning and initial squeezing angle allows the BNS range to reach 93.0 Mpc under the current FC bandwidth. By varying all three FC parameters the maximum BNS range is found to be 95.7 Mpc. This gives a qualitative description of the increase of sensitivity of the current VIRGO detector in DRSE setup brought by FDS.

Contents

1 Introduction

Ever since Einstein linearlized his theory of general relativity (GR) to obtain a wave-like solution[1, 2], debates has lasted for decades about whether gravitational wave (GW) is real or simply an artefact from coordinate choice. Tremendous interllectual effort was spent on proving the reality of GW[3, 4]. The discovery of Hulse-Taylor pulsar in 1974 indirectly confirmed the existence of GW by showing the match between the observed orbital decay of the binary pulsar and the one predicted by gravitational radiation loss.[5]. This brought a renaissance to the field that just went through the setback of null results of resonant bar detectors first proposed by the pioneer of GW detection Joseph Weber[6]. Then the idea of using interferometers to search for GW signal started to emerge and solidify[7, 8]. Starting from the 1990s kilometer-scale GW interferometers began to be built, such as the French-Italian collaboration project VIRGO[9], and the joint MIT-Caltech project LIGO[8, 10]. After decades of construction and upgradation, the detectors gradually reached the desired sensitivity and the first GW signal was detected in September 2015[11], marking a remarkable triumph of a century of theoretical investigation and half a century of relentless experimental commitment[12]. Up to the last observation run O3 ended in 2020, about 90 GW events have been detected[13]. The advent of GW astronomy offers new ways to explore questions on fundamental theories of gravity, astrophysics, cosmology and nuclear physics. Further test of GR can be conducted and alternative theories of gravitation can be constrained[14, 15]. An independent measurement of Hubble parameter can be carried out as attempts to ease the Hubble tension that appears over recent years[16, 17]. New light can be shed on the understanding of equation of state of dense matter like neutron stars[14, 18]. The list of exciting questions continues.

However on the experimental side, since the relative distorsion of distance $\Delta L/L$ of two freely falling masses in the presence of GW reaching Earth is typically 10^{-21}, measuring this feeble GW signal is an extremely challenging task even for km-size interferometers like VIRGO which will be the focus of this work. The VIRGO detector first completed its construction at Cascina near Pisa, Italy in 2003 and started joint data taking with LIGO in 2007[12]. The infrastructure of initial VIRGO consists of 3-km Michelson interferometer with ultra-high vacuum tubes enclosing the arms. Mode cleaners at the input and output port are used to select the TEM00 mode of the laser. Mirrors are suspended by a chain of pendula to isolate them from sesmic noise. Continuous control of mirror position and angle ensures to lock the working point on the dark fringe. Power recycling (PR) is installed to increase circulating power in the arms. Fabry-Pérot (FP) cavities are implemented in the arms to increase the effective arm length[9, 19]. The sensitivity, evaluated by binary neutron star (BNS) range[1] is around 4 Mpc at this stage[19]. The second upgrade leading to Advanced VIRGO (AdV) took place from 2009 to 2017. Fused silica grades, low loss and low absorption coating are introduced to the new mirrors to reduce thermal noises and optical losses. New payload designs are developed to be compatible with the super attenuators to reduce the sesmic noise[21]. Frequency independent squeezing (FIS) is also introduced in AdV for the O3 run. During O3 AdV has reached a

---

[1] A comoving distance of the farthest BNS coalescence probable by the detector given a signal-to-noise ratio of 8, averaged over volume and orientation. For details see[20].

BNS range up to 60 Mpc. After O3, AdV was upgraded into AdV+ planned for the O4 run in 2023 which is currently under commissioning at the time of writing, with a target sensitivity of around 80 to 90 Mpc for phase I of AdV+. Apart from the newly installed signal recycling (SR) mirror, another novel feature is the frequency dependent squeezed vacuum[22], allowing to supress the quantum noise over the whole frequency range. This is the topic of the present internship project.

Studying the quantum noise not only helps boosting the sensitivity of the detectors, but also opens the door to exploring the richness of quantum physics. The quantum noise has two sources: shot noise arising from the randomness of the number of photons hitting the test mass mirrors, and radiation pressure noise due to the motion of mirror brought by the laser impinging on it[23]. In conventional interferometers these two effects yield that there exists an optimal power where the sensitivity reaches the minimal envelop bounded by the standard quantum limit (SQL) at a specific frequency. Increasing the laser power will reduce shot noise but increase the radiation noise and vice versa. The SQL is an intrinsic limitation imposed by the law of quantum mechanics, namely Heisenberg uncertainty principle for light used in the detection. The existence of SQL was first discussed by Braginsky[24]. Its origin and application in GW interferometers was explored by Caves *et al.*[25]. Conventional interferometers require un unrealistically high input power for the sensitivity to come close to SQL. The dual recycled interferometers, i.e., PR and SR recycled ones, remedies this and create resonant dips in the sensitivity curves, allowing even to beat SQL in some certain ranges[26]. On top of this sophisticated improvement of interferometers, a more desirable reduction of quantum noise over all frequency range is realised by the technique of squeezing[27], or in its more recent form, frequency dependent squeezing (FDS). The basic idea of FDS is to inject a squeezed vacuum of light field from the dark port of interferometer by using filter cavity (FC), so as to counteract the ponderomotive rotation of quantum noise ellipse brought by the interferometer[28]. In the case where the SR cavity detuning phase is set to $\pi/2$, i.e., Resonant Sideband Extraction (RSE) regime, the optimal FDS can be realised by tuning the parameters of one FC[29]. This strategy has been well demonstrated in LIGO. But the RSE is not well adapted to AdV because higher order modes generated in the interferometer can leak out towards the photodetector due to marginal stability of SR mirror in VIRGO, undermining the detection. A possible solution is to operate in the detuned RSE (DRSE) regime. This brings the question: how well can one FC augment the performance of the detector? Moreover for future generation GW detector such as Einstein Telescope (ET) planned to be operating around 2038, both RSE and DRSE regime are considered. While having more than one FC allows to achieve better FDS in the latter, losses and degradation of squeezing brought by an extra FC should also be taken into account to evaluate the pros and cons. Hence the objective of this work is on numerical optimization over FC parameters to achieve optimal FDS for AdV+ to detect binary GW events. In principle the same strategy can be applied to ET as well. This will certainly provide some guidance for the the coming observational runs and instrumental construction.

The report is organized as follows: in section 2, basic concepts in quantum optics such as coherent and squeezed state, are presented. The input-output relation is derived for the Michelson interferometer and the notion of spetral density is introduced. Section

discusses FDS in both RSE and DRSE regime in LIGO-VIROGO-like interferometers, using both analytic and numerical approach. Finally section summarizes the results and provide some outlook for the next step in this research.

2   Quantum noise in interferometric detectors

First the monochromatic light field is discussed, since it has the simplest formalism such as quantization, coherent state, squeezing and quantum fluctuation. Then these concepts are generalised to light field spanning the whole continuous frequency range. The mathematical formalism is a bit more complicated but the essential ideas are the same. The latter will be eventually applied to interferometers to illustrate the concept of quantum noise.

2.1   Basic notions of quantum optics

The plane wave solution to Maxwell equations in free space is

$$\vec{E}(t,\vec{r}) = \vec{E}_0 \left[a\ e^{-i(\omega t - \vec{k}\cdot\vec{r})} + a^*\ e^{i(\omega t - \vec{k}\cdot\vec{r})} \right], \tag{2.1}$$

which describes a monochromatic wave with a fixed angular frequency ω and wave number k. The polarisation vector $\vec{E}_0$ absorbs the strength of the field. In the following the arrow over the light field is dropped for simplicity, but one should keep in mind that this is a vector in Cartesian coordinate with only 2 degrees of freedom since $\vec{k}\cdot\vec{E} = 0$. Choose the direction of $\vec{k}$ to be the z axis and after quantisation, the light field is promoted to a hermitian operator on a Hilbert space spanned by the state vectors of light as a quantum system, which is written as

$$\hat{E}(t,z) = E_0 \left[\hat{a}\ e^{-i(\omega t - kz)} + \hat{a}^\dagger\ e^{i(\omega t - kz)} \right]. \tag{2.2}$$

$\hat{a}$ and $\hat{a}^\dagger$ are the creation and annihilation operator of this monochromatic photon and satisfies the commutation relation

$$[\hat{a}, \hat{a}^\dagger] = 1. \tag{2.3}$$

All other commutators vanish. From now on the spatial dependence of the light field will be omitted, since a free propogation of the light field from z to $z+l$ corresponds to changing $\hat{E}(t,z)$ to $\hat{E}(t-l/c, z)$. An alternative description of the light field is through the quadrature operators, defined as

$$\hat{a}_1 = \frac{1}{\sqrt{2}}\left(\hat{a} + \hat{a}^\dagger\right) \qquad \hat{a}_2 = \frac{1}{\sqrt{2}i}\left(\hat{a} - \hat{a}^\dagger\right), \tag{2.4}$$

where $\hat{a}_1$ and $\hat{a}_2$ are called amplitude and phase quadrature respectively. Then the light field in (2.2) can be written as

$$\hat{E}(t) = \sqrt{2}E_0 \left(\hat{a}_1 \cos\omega t + \hat{a}_2 \sin\omega t\right), \tag{2.5}$$

with the non-trivial commutation relation $[\hat{a}_1, \hat{a}_2] = i$. In this way the observable light field is expressed in terms of observables, the quadratures, since they are hermitian.

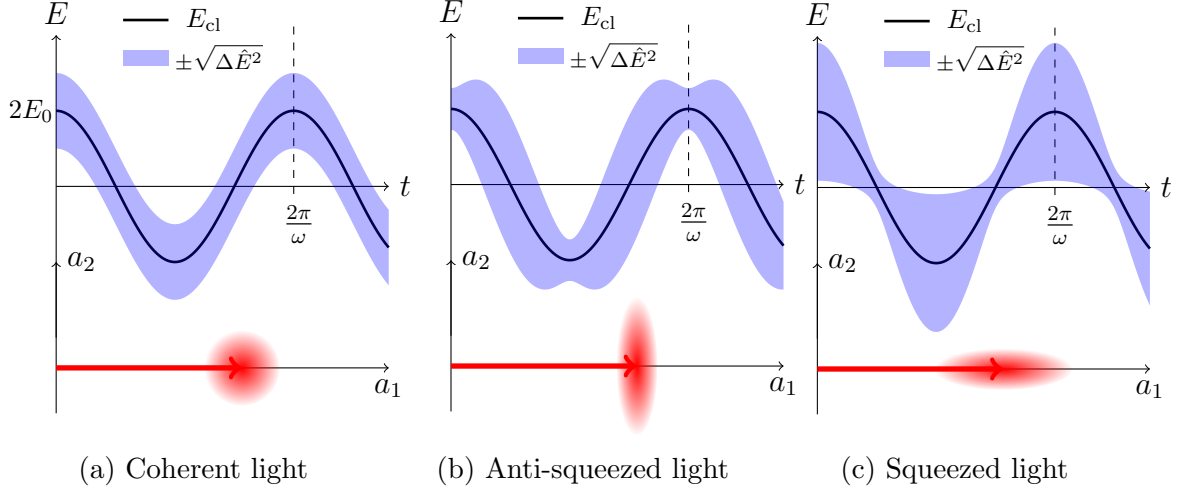(a) Coherent light   (b) Anti-squeezed light   (c) Squeezed light

Figure 1: The coherent and coherent-squeezed monochromatic light in the phasor picture. The lower part displaying the quadrature planes are not shown to scale as the upper pannels for the convience of plotting and illustration. The coherent amplitude is chosen to be $\alpha = 1$ so that the classical field represented by the solid line is $E_{\text{cl}}(t) = 2E_0 \cos\omega t$ according to (2.7). The squeezing parameter is chosen as such that $\phi = 0$ and $\chi = r \in \mathbb{R}$. Here $r > 0$ for (b) and $r < 0$ for (c). In either case the quantum fluctuation oscillates with a frequency twice as that of the classical light field, as a result of (2.11). The quadrature plane can be regarded as a complex plane to visualize the coherent amplitude, which is nonthing but the classical phasor in the rotating frame with the same rotating frequency of the light field. The quantum fluctuation can be regarded as random phasors superimposed on top of the classical field represented by the bold red arrow. By tuning the squeezing parameter χ one can ontain different patterns of quantum fluctuations. This image was first produced by Caves in [27].

The coherent state $|\alpha\rangle$ is defined to be the eigenstate of the annihilation operator, i.e., $\hat{a}|\alpha\rangle = \alpha|\alpha\rangle$ for some $\alpha \in \mathbb{C}$. It can be realised by acting on the vacuum state with the coherent operator $\hat{D}(\alpha)$, which is defined as a unitary operator as the following

$$\hat{D}(\alpha)|0\rangle \equiv \exp\left(\alpha\hat{a}^\dagger - \alpha^*\hat{a}\right)|0\rangle = |\alpha\rangle. \tag{2.6}$$

If the coherent state of light is physically obtained, we'll be interested in the expectation and variance of our observable under this state, which in this case is the light field (2.5). But we can adopt the Heisenberg picture[2] and regard the change from vacuum to coherent state as the change of operator $\hat{E}_\alpha(t) = \hat{D}^\dagger(\alpha)\hat{E}(t)\hat{D}(\alpha)$. It can be easily shown using the commutation relation, that the coherent light field is express as

$$\hat{E}_\alpha(t) = E_0\left[(\alpha + \alpha^*)\cos\omega t - i(\alpha - \alpha^*)\sin\omega t\right] + \hat{E}(t) \equiv E_{\text{cl}}(t) + \hat{E}(t). \tag{2.7}$$

---

[2]The term Heisenberg picture and Schrödinger picture are used even if the unitary operator under discussion is not time evolution operator. It's the case for the coherent operator as well as the squeeze and rotation operators to be introduced later.

4

This expression has a clear physical meaning: a coherent light is nothing but a classical light field superimposed by quantum fluctuation. A simple calculation of the vacuum expectation and variance shows that

$$\langle \hat{E}_\alpha(t) \rangle = \langle 0| \, \hat{E}_\alpha(t) \, |0\rangle = E_{\text{cl}}(t) \tag{2.8a}$$

$$\langle \Delta \hat{E}_\alpha(t)^2 \rangle = \langle 0| \left(\hat{E}_\alpha(t) - E_{\text{cl}}(t) \right)^2 |0\rangle = E_0^2 = \text{const} \tag{2.8b}$$

Another important operator is the squeeze operator, which is again a unitary operator but defined as

$$\hat{S}(\chi) \equiv \exp\left(\frac{1}{2} \chi^* \hat{a}^2 - \frac{1}{2} \chi \hat{a}^{\dagger 2} \right), \tag{2.9}$$

where the squeezing parameter is defined by $\chi = r e^{2i\phi} \in \mathbb{C}$. Then the squeezed coherent light field is

$$\begin{aligned}
\hat{E}_{\alpha,\chi}(t) &= \hat{S}^\dagger(\chi) \hat{E}_\alpha(t) \hat{S}(\chi) = E_{\text{cl}}(t) + \hat{S}^\dagger(\chi) \hat{E}(t) \hat{S}(\chi) \\
&= E_{\text{cl}}(t) + \sqrt{2} E_0 \left[(\cosh r - \cos 2\phi \sinh r) \hat{a}_1 - \sin 2\phi \sinh r \ \hat{a}_2 \right] \cos \omega t \\
&\quad + \sqrt{2} E_0 \left[- \sin 2\phi \sinh r \ \hat{a}_1 + (\cosh r + \cos 2\phi \sinh r) \hat{a}_2 \right] \sin \omega t.
\end{aligned} \tag{2.10}$$

The vacuum expectation for the squeezed coherent light is still the classical field expressed in (2.7), but the variance is no longer a constant. Instead it's an oscillation with twice the frequency as the classical field

$$\langle \Delta \hat{E}_{\alpha,\chi}(t)^2 \rangle = E_0^2 \left[\cosh 2r - \sinh 2r \cos(2\omega t - 2\phi) \right]. \tag{2.11}$$

A graphical representation of these results are given in Fig 1. The application of these notions in GW detection is only to consider all possible sideband frequencies. In terms of mathematical formalisms, the observable light field is summed over a continuous range of frequencies. The coherent amplitude $\alpha(\Omega)$ and the squeeze parameter $\chi(\Omega) = r(\Omega) \exp(2i\phi(\Omega))$ becomes functions of frequency. The analysis is quite similar to the case of monochromatic light, with the classical field replaced by the GW signal and the quantum variance interpreted as the quantum noise. In particular, the non-zero variance $\langle \hat{a}_i^2 \rangle$, $(i = 1, 2)$ which arises from photon number fluctuation, accounts for the shot noise. And everything is done in a "frequency-wise" way. But a new tool, called two-photon formalism[30, 31], has to be implemented to consider sidebands around a carrier laser frequency.

2.2 From monochromatic light to sidebands and two-photon formalism

In Fig 1, the classical light field is represented as a fixed phasor arrow in the co-rotating frame of the light. In the presence of modulation, this light field is called the carrier. An amplitude modulation causes the arrow end to move back and forth along the amplitude axis a_1. A phase modulation causes the arrow end to go back and forth vertically, making the arrow swing around a_1 axis. This effect is due to superposition of

the carrier phasor arrow and the sideband phasor arrows[32]. The modulation frequency is the sideband frequency and simply the GW frequency in the the case of GW detection. The mathematical formalism to deal with sideband for classical field is well represented by the modulation factors entering the functions representing the light field such as (2.1). But the tool to describe the sideband picture for the quantum light field will have to rely on the two-photon formalism proposed by Caves and Schumaker in [30, 31], which is presented below.

Consider a carrier laser beam of frequency ω_0. Its quantum fluctuation should cover a whole range of frequency[28]

$$\hat{E}(t) = \int\limits_0^\infty \frac{\mathrm{d}\omega}{2\pi} \sqrt{\frac{2\pi\hbar\omega}{\mathcal{A}c}} \hat{a}_\omega e^{-i\omega t} + \text{h.c.} = \hat{E}^+(t) + \text{h.c.}, \tag{2.12}$$

where $\mathcal{A}$ is the cross section of the laser beam and c is the speed of light. The non-trivial commutation relation becomes $[\hat{a}_\omega, \hat{a}_{\omega'}^\dagger] = 2\pi\delta(\omega - \omega')$. If only the sidebands around carrier frequency ω_0 matter, meaning only the sidebands with frequency $\Omega \ll \omega_0$ contributes to the integration, then the positive frequency part can be approximated as

$$\hat{E}^+(t) = \frac{1}{2} \int\limits_{-\omega_0}^{+\infty} \frac{\mathrm{d}\Omega}{2\pi} \sqrt{\frac{2\pi\hbar(\omega_0 + \Omega)}{\mathcal{A}c}} \hat{a}_{\omega_0+\Omega} \, e^{-i(\omega_0+\Omega)t} + \frac{1}{2} \int\limits_{\omega_0}^{-\infty} \frac{\mathrm{d}\Omega}{2\pi} \sqrt{\frac{2\pi\hbar(\omega_0 - \Omega)}{\mathcal{A}c}} \hat{a}_{\omega_0-\Omega} \, e^{-i(\omega_0-\Omega)t}$$

$$\approx \sqrt{\frac{2\pi\hbar\omega_0}{\mathcal{A}c}} e^{-i\omega_0 t} \int\limits_0^\infty \frac{\mathrm{d}\Omega}{2\pi} \left(\hat{a}_+ \, e^{-i\Omega t} + \hat{a}_- \, e^{i\Omega t} \right). \tag{2.13}$$

The approximation is done by admitting $\omega_0 \pm \Omega \approx \omega_0$ to take out the squareroot, approximating the ω_0 in the integration limits by ∞ and defining $\hat{a}_\pm \equiv \hat{a}_{\omega_0\pm\Omega}$. Rewriting the integrated operator as time dependent annihilation operator in the second line, the quantum fluctuation in (2.12) can be written as

$$\hat{E}(t) = \sqrt{\frac{2\pi\hbar\omega_0}{\mathcal{A}c}} \left(\hat{a}(t) \, e^{-i\omega_0 t} + \hat{a}^\dagger(t) \, e^{i\omega_0 t} \right), \tag{2.14}$$

in complete analogy with (2.2), with the easily verified non-trivial commutation relation $[\hat{a}(t), \hat{a}^\dagger(t')] = \delta(t - t')$ again analogous to (2.3) and E_0 identified with $\sqrt{(2\pi\hbar\omega_0)/(\mathcal{A}c)}$. So we can almost proceed as before, except that the creation and annihilation operators, as well as the two quadrature operators are now time dependent and cover all frequencies.

$$\hat{E}(t) = \sqrt{\frac{4\pi\hbar\omega_0}{\mathcal{A}c}} \left[\hat{a}_1(t) \cos\omega_0 t + \hat{a}_2(t) \sin\omega_0 t \right]$$

$$= \sqrt{\frac{4\pi\hbar\omega_0}{\mathcal{A}c}} \left[\cos\omega_0 t \int\limits_0^\infty \frac{\mathrm{d}\Omega}{2\pi} \left(\hat{a}_1(\Omega) \, e^{-i\Omega t} + \text{h.c.} \right) + \sin\omega_0 t \int\limits_0^\infty \frac{\mathrm{d}\Omega}{2\pi} \left(\hat{a}_2(\Omega) \, e^{-i\Omega t} + \text{h.c.} \right) \right]. \tag{2.15}$$

But notice a crucial difference with the monochromatic light: the quadrature operators in *frequency* domain consist of creation and annihilation operators from *both* upper and

lower sideband, i.e.,

$$\hat{a}_1(\Omega) = \frac{1}{\sqrt{2}}(\hat{a}_+ + \hat{a}_-^\dagger) \qquad \hat{a}_2(\Omega) = \frac{1}{\sqrt{2}i}(\hat{a}_+ - \hat{a}_-^\dagger). \tag{2.16}$$

This is the reason why such a formalism is called the two-photon formalism. The non-trivial commutation relation reads

$$[\hat{a}_1(t), \hat{a}_2(t')] = i\delta(t - t') \qquad [\hat{a}_1(\Omega), \hat{a}_2^\dagger(\Omega')] = 2\pi i \delta(\Omega - \Omega'), \tag{2.17}$$

again in analogy with $[\hat{a}_1, \hat{a}_2] = i$ in the monochromatic case.

The coherent operator and squeeze operator become operator-valued functionals, with a coherent function (a function of frequency, in contrast to coherent amplitude as a c-number before) and a squeeze function as inputs. Formally they are defined as[28, 30, 31, 33]

$$\hat{D}[\alpha(\Omega)] \equiv \exp\left[\int_0^\infty \frac{d\Omega}{2\pi}\left(\alpha(\Omega)\hat{a}_\Omega^\dagger - \alpha^*(\Omega)\hat{a}_\Omega\right)\right], \tag{2.18}$$

$$\hat{S}[\chi(\Omega)] \equiv \exp\left[\int_0^\infty \frac{d\Omega}{2\pi}\left(\chi^*(\Omega)\hat{a}_+\hat{a}_- - \chi(\Omega)\hat{a}_+^\dagger\hat{a}_-^\dagger\right)\right]. \tag{2.19}$$

Just like in the analysis of monochromatic light, the classical carrier light field can be obtained from the vacuum field by shifting it by $\alpha(\Omega)$. In a standard laser the coherent function is $\alpha(\Omega) = \sqrt{2}\pi\bar{a}\delta(\Omega - \omega_0)$, with $\bar{a} = \sqrt{(2P_0)/(\hbar\omega_0)}$ and P_0 being the input laser power, since the carrier laser contains only a single frequency ω_0. An analogous calculation shows[33]

$$\hat{E}_\alpha(t) = \left(\sqrt{\frac{2P_0}{\hbar\omega_0}} + \hat{a}_1(t)\right)\cos\omega_0 t + \hat{a}_2(t)\sin\omega_0 t, \tag{2.20}$$

with the time dependent quadrature operators $\hat{a}_{1,2}(t)$ read out from (2.15) and the unit system chosen as $\sqrt{2}E_0 = \sqrt{(4\pi\hbar\omega_0)/(\mathcal{A}c)} = 1$. Again an interpretation of classical light field superimposed by quantum fluctuation is endowed on such an expression, except now the quantum part contains contribution from all sideband frequencies. It's hardly worth the pain to work out the squeezed light field in time domain, but the physics is that in frequency domain, the quadrature operator at each frequency value Ω is squeezed by the squeezing parameter $\chi(\Omega) = r(\Omega)\exp(2i\phi(\Omega))$ at that frequency, in precisely the same manner as discussed in section 2.1.

2.3   Input-Output relations and noise spectral density

The physics of quantum noise in ground based GW detectors is mostly contained in the input-ouput relation, i.e., the linear combination of the output quadrature operators in terms of the input quadrature operators, for the Michelson interferometer shown in Fig 2a. The strain equivalent noise spetral density will be derived from this relation. This will be the focus of this subsection. More sophisticated optical configuration, such

as the one shown in Fig 4a, simply gives rise to a different response for the quadratures with more complex frequency dependent linear coeffecients. For simplicity, the unit in this subsection is chosen as $\sqrt{(4\pi\hbar\omega_0)/(\mathcal{A}c)} = 1$. The notations for light field of different modes are defined in Fig 2a. The optical lossse are negelected altogether here.

(a) Configuration of Michelson interferometer

(b) Quantum noise strain for Michelson Interferometer

Figure 2: The configuration and quantum noise in simple Michelson interferometer. On the left panel BS stands for beam splitter. The convention is that light reflected from the bold side of the BS suffers a π phase shift. ETM stands for end test mass, meaning the end mirrors of the two arms labelled by A and B. The arm lengths are the same. The dashed lines are the position of the mirror faces hit by laser when a + mode GW transmits through the plane perpendicularly. On the right panel, sensitivity curves for quantum noise are plotted from (2.36), with parameters $m = 40$ kg and $L = 4$ km. It can be seen that to approach the SQL in an actual interferometer, unrealistically high input power is needed. Also shown here are the error ellipses of output quadratures in frequency domain for $P_0 = 10^8$ W and a few frequency values. Such a ponderomotive squeezing is the response of the interferometer configuration. It's plotted from (2.34) and (2.35).

The BS is a 50%-50% one, meaning the laser immediately after the BS is

$$\hat{E}_{inA}(t) = \frac{1}{\sqrt{2}}\hat{E}_{in}(t) - \frac{1}{\sqrt{2}}\hat{E}_Q(t) \qquad \hat{E}_{inB}(t) = \frac{1}{\sqrt{2}}\hat{E}_{in}(t) + \frac{1}{\sqrt{2}}\hat{E}_Q(t) \qquad (2.21)$$

and the output light field going towards the photodiode readout is

$$\hat{E}_{out}(t) = -\frac{1}{\sqrt{2}}\hat{E}_{outA}(t) + \frac{1}{\sqrt{2}}\hat{E}_{outB}(t), \qquad (2.22)$$

where $\hat{E}_{out\,j}(t)$ $(j = A, B)$ is related to their input field by $\hat{E}_{out\,j}(t) = \hat{E}_{in\,j}(t - 2L/c - 2x_j/c)$. From these linear relations the output light field can be written as
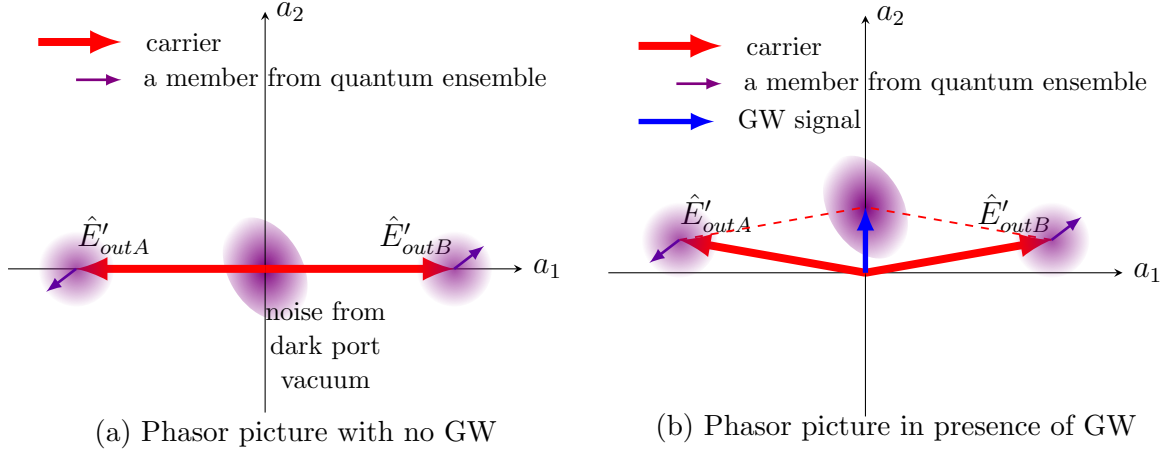
$$\hat{E}_{out}(t) = \frac{1}{2}\hat{E}_Q(t-2\tau-\frac{2x_A}{c}) + \frac{1}{2}\hat{E}_Q(t-2\tau-\frac{2x_B}{c}) - \frac{1}{2}\hat{E}_{in}(t-2\tau-\frac{2x_A}{c}) + \frac{1}{2}\hat{E}_{in}(t-2\tau-\frac{2x_B}{c}).$$
$$(2.23)$$

(a) Phasor picture with no GW
(b) Phasor picture in presence of GW

Figure 3: The phasor picture. $\hat{E}'_{outj}$ is the mode immediately coming out of BS towards the photodiode. This is not marked in Fig 2a. (a) shows the situation in the absence of GW. The light coming from the two arms differ by a phase shift of π. This is the case for the classical carrier light and the quantum fluctuation from the bright port, thus explaining the absence of contribution to quantum noise from the bright port when the working point is on the dark fringe. In (b) when GW signal passes by, the classical carrier is frequency modulated. Their superposition produces the GW signal. In this case the quantum fluctuation from the bright port no longer exactly cancel since the arms are no longer of the same length, but this effect is of second order infinitesimal and can be neglected. The quantum noise from dark port vacuum fluctuation are shown as a tilted ellipse at some sideband frequency. The drawings are not shown to scale for the convenience of visualization.

The x_j $(j = A, B)$ in the argument should be thought of as $x_j(t - \tau)$ to account for the single trip of light travelling from BS to the ETM. In practice the two arms are designed to be at resonance with the carrier, meaning $\omega_0 L/c = \omega_0 \tau = n\pi$, $n \in \mathbb{Z}$. Then do a Taylor expansion, keeping in mind that $\hat{a}_{in\,i}$, $\hat{a}_{Q\,i}$, $(i = 1, 2)$ and x_j are already to first order and neglecting higher order terms,

$$\hat{E}_{in}(t - 2\tau - 2x_j/c) = [\hat{a}_{in1}(t - 2\tau) + \bar{a}] \cos \omega_0 t + \left[\hat{a}_{in2}(t - 2\tau) + \frac{2\omega_0 \bar{a}}{c} x_j(t - \tau) \right] \sin \omega_0 t. \tag{2.24}$$

$$\hat{E}_Q(t - 2\tau - 2x_j/c) = \hat{a}_{Q1}(t - 2\tau) \cos \omega_0 t + \hat{a}_{Q2}(t - 2\tau) \sin \omega_0 t \tag{2.25}$$

Plugging these back into (2.23), the Taylor expanded output field will be

$$\hat{E}_{out}(t) = \hat{a}_{Q1}(t - 2\tau) \cos \omega_0 t + \left[\hat{a}_{Q2}(t - 2\tau) + \frac{\omega_0 \bar{a}}{c} x_{BA}(t - \tau) \right] \sin \omega_0 t, \tag{2.26}$$

where $x_{BA} = x_B - x_A$. Already, some physics can be extracted from this expression. The output field does not contain $\bar{a} \cos \omega_0 t$ from the carrier laser, which means the apparatus is operated on the dark fringe. This makes sense since in our theoretical modelling the two arms are of the same length and there is a π phase shift for light reflected by the BS when coming back from arm A. And at least for shot noise, only the vacuum fluctuation coming from the dark port will contribute. This can be imagined solely based on the phasor picture Fig 3. For light coming from the bright port, the two phasors from two

arms exactly differ by a phase rotation of π, be them classical phasors or the random quantum phasors added on top of them. Based on this picture, the radiation pressure noises from quantum fluctuation of the carrier should also cancel out. The subsequent calculation will only verify this physical intuition.

However, if x_{BA} in (2.26) is only treated as a classical variable arising from tidal deformation of GW, the radiation pressure noise will be completely omitted. Actually, the displacement of the mirrors should also be treated as a quantum observable[3] $\hat{x}_{BA} = \hat{x}_B - \hat{x}_A$. By definition, analogous to the input laser field expressed in (2.20), for the output field

$$\hat{E}_{out}(t) = \hat{a}_{out1}(t)\cos\omega_0 t + \hat{a}_{out2}(t)\sin\omega_0 t, \tag{2.27}$$

in which both quadrature operators can contain some classical signal in general. Comparing with (2.26) gives us the time domain input-output relation

$$\hat{a}_{out1}(t) = \hat{a}_{Q1}(t - 2\tau) \tag{2.28a}$$

$$\hat{a}_{out2}(t) = \hat{a}_{Q2}(t - 2\tau) + \frac{\omega_0\bar{a}}{c}\hat{x}_{BA}(t - \tau). \tag{2.28b}$$

This means the GW signal is only contained in the phase quadrature, again in agreement with the phasor picture Fig 3. To convert the input-output relation to frequency domain, notice that the design of the mirrors is such that they are suspended by long enough wires such that the characteristic frequency of the suspension (like in the case of a pendulum) is much smaller than the characteristic GW frequency 10 Hz to 10 kHz, $f_{susp} \ll \Omega$, so they can be treated as free test masses. Suppose there is a GW of $+$ mode travelling perpendicularly through Fig 2a, the equation of motion for the test masses can be written as[34]

$$m\ddot{\hat{x}}_j = \hat{F}_{rpj}(t) + \frac{1}{2}\text{sgn}(j)m\ddot{h}(t)L, \tag{2.29}$$

with $\text{sgn}(A) = -1$, $\text{sgn}(B) = 1$ and m being the mirror mass. The radiation pressure force is given by

$$\hat{F}_{rpj} = 2\frac{\mathcal{A}}{4\pi}\overline{\hat{E}_{inj}^2(t - \tau)} \tag{2.30}$$

A bar means average over time, which means ignoring rapidly varying terms such as those oscillating with carrier frequency. Based on (2.21),

$$m\ddot{\hat{x}}_{BA}(t) = \frac{\mathcal{A}\bar{a}}{2\pi}\hat{a}_{Q1}(t - \tau) + m\ddot{h}(t)L. \tag{2.31}$$

The physics here is that the radiation pressure noise, again only arises from vacuum field from the dark port and not from the bright port. This should be expected since no matter how randomly the photon pushes the mirrors, they push them in the same way. And due to the extra π phase shift of the BS for $\hat{E}_{outA}$, the detector does not "see" this random pushing. But this is not the case for $\hat{E}_Q$ entering through the dark port because of a

---

[3]It is not clear what it means for operators to be the input of an operator-valued function as $\hat{E}_{out}$ in the above expressions, but the Taylor expansion will not be affected since $\hat{x}_j \in \mathcal{H}_j$, which should commute with observables living in the Hilbert space of light. There is no ordering issue when doing Taylor expansion.

second reflection by the BS. Combining (2.28) and (2.31), the input-output relation in the frequency domain can finally be written as

$$\begin{pmatrix} \hat{a}_{out1}(\Omega) \\ \hat{a}_{out2}(\Omega) \end{pmatrix} = e^{2i\Omega\tau} \begin{pmatrix} 1 & 0 \\ -\kappa(\Omega) & 1 \end{pmatrix} \begin{pmatrix} \hat{a}_{Q1}(\Omega) \\ \hat{a}_{Q2}(\Omega) \end{pmatrix} + \sqrt{2\kappa}e^{i\Omega\tau} \begin{pmatrix} 0 \\ \frac{h(\Omega)}{h_{\mathrm{SQL}}(\Omega)}, \end{pmatrix} \qquad (2.32)$$

where $\kappa(\Omega)$ and $h_{\mathrm{SQL}}(\Omega)$ are defined as

$$\kappa(\Omega) = \frac{4P_0\omega_0}{mc^2\Omega^2} \qquad h_{\mathrm{SQL}}(\Omega) = \sqrt{\frac{4\hbar}{m\Omega^2 L^2}}. \qquad (2.33)$$

The diagonal terms in the transfer matrix in (2.32) contribute to shot noise while the off diagonal term contribute to radiation pressure noise. The transfer matrix demonstrates a kind of frequency dependent squeezing and rotation brought solely by the interferometer, dubbed *ponderomotive* squeezing. It can be verified that[28]

$$\begin{pmatrix} \hat{a}_{out1}(\Omega) \\ \hat{a}_{out2}(\Omega) \end{pmatrix} = e^{2i\Omega\tau} \hat{S}^\dagger(r,\varphi)\hat{R}^\dagger(\theta) \begin{pmatrix} \hat{a}_{Q1}(\Omega) \\ \hat{a}_{Q2}(\Omega) \end{pmatrix} \hat{R}(\theta)\hat{S}(r,\varphi), \qquad (2.34)$$

with frequency dependent angles and squeezing amplitude

$$\theta = \arctan\left(\kappa(\Omega)/2\right), \quad \varphi = \frac{1}{2}\operatorname{arccot}\left(\kappa(\Omega)/2\right), \quad r = \operatorname{arcsinh}\left(\kappa(\Omega)/2\right). \qquad (2.35)$$

The output error ellipse of such ponderomotive squeezing is represented in Fig 2b, for a chosen set of parameters. Notice that at high enough frequencies the ellipse almost becomes a circle. It's a sign that a white noise dominates at high frequencies, which is nothing but the shot noise.

The strength of the quantum noise is measured by the double-sided spectral density[4] for $\hat{a}_{out2}(\Omega)$. Converting to strain equivalent noise spectral density

$$S^h = \frac{h_{\mathrm{SQL}}^2}{2\kappa(\Omega)}\left(1+\kappa^2(\Omega)\right) = \frac{h_{\mathrm{SQL}}^2}{2}\left(\frac{1}{\kappa}+\kappa\right) \geq h_{\mathrm{SQL}}^2(\Omega). \qquad (2.36)$$

The upshot is that, there exists a standard quantum limit for the sensitivity of simple Michelson interferometer, which is reached by an optimal input laser power given a fixed experimental setup. For $m = 40$ kg, carrier wavelength being $\lambda = 1064$ nm and a sideband angular frequency $\Omega = 100$ Hz, the optimal power is estimated to be $P_0 \approx 5\times10^6$ W, which is way beyond any comercially realisable laser. This is why more complex configuration, such as PR and arm FP cavities are introduced, as in Fig 4a. In either case, the additional structures simply change the input-output relation by the relation for the modes into and out of the additional cavities. Details can be found in [26, 28, 29]. A general expression for the input-output relation for advance detectors can be formally written as

$$\begin{pmatrix} \hat{b}_1(\Omega) \\ \hat{b}_2(\Omega) \end{pmatrix} = \frac{1}{M}\left[\boldsymbol{T}(\Omega)\begin{pmatrix} \hat{a}_1(\Omega) \\ \hat{a}_2(\Omega) \end{pmatrix} + \bar{\boldsymbol{s}}(\Omega)h(\Omega)\right]. \qquad (2.37)$$

---

[4]The double-sided spectral density for any pair of observables $\hat{\mathcal{O}}_1$ and $\hat{\mathcal{O}}_2$ denoted as $S_{\mathcal{O}_1\mathcal{O}_2}$ is defined as $\frac{1}{2}S_{\mathcal{O}_1\mathcal{O}_2}\delta(\Omega-\Omega') \equiv \frac{1}{2\pi}\langle 0|\,\mathcal{O}_1(\Omega)\mathcal{O}_2(\Omega')\,|0\rangle_{\mathrm{sym}} = \frac{1}{2\pi}\langle 0|\,\frac{1}{2}\{\mathcal{O}_1(\Omega)\mathcal{O}_2(\Omega')\}\,|0\rangle$. This is the generalisation of quantum cross correlation to the observables depending on a continuous range of frequency, which in the case of $\mathcal{O}_1 = \mathcal{O}_2$ and $\langle\mathcal{O}_1\rangle = 0$ is simply the variance. It, as a measure of noise strength, is simply the generalisation of the variance discussed for the monochromatic light in subsection 2.1.

For dual recycled interferometers with arm FP cavities, the coefficient M, matrix $\boldsymbol{T}$ and vector $\bar{\boldsymbol{s}}$ can be derived[26, 29] as

$$T_{11,22} = e^{2i\Phi}\left[(1 + r_{\text{SR}}^2)(\cos 2\phi_{\text{SR}} + \frac{\kappa}{2}\sin 2\phi_{\text{SR}}) - 2r_{\text{SR}}\cos 2\Phi\right] \tag{2.38a}$$

$$T_{12} = -e^{2i\Phi}t_{\text{SR}}^2(\sin 2\phi_{\text{SR}} + \kappa\sin^2\phi_{\text{SR}}), \quad T_{21} = e^{2i\Phi}t_{\text{SR}}^2(\sin 2\phi_{\text{SR}} - \kappa\cos^2\phi_{\text{SR}}). \tag{2.38b}$$

$$M = 1 + r_{\text{SR}}^2 e^{4i\Phi} - 2r_{\text{SR}}e^{2i\Phi}\left(\cos\phi_{\text{SR}} + \frac{\kappa}{2}\sin 2\phi_{\text{SR}}\right). \tag{2.39}$$

$$\bar{s}_1 = -\frac{\sqrt{2\kappa}}{h_{\text{SQL}}}t_{\text{SR}}(1 + r_{\text{SR}}e^{2i\Phi})\sin\phi_{\text{SR}}, \qquad \bar{s}_2 = -\frac{\sqrt{2\kappa}}{h_{\text{SQL}}}t_{\text{SR}}(-1 + r_{\text{SR}}e^{2i\Phi})\cos\phi_{\text{SR}}. \tag{2.40}$$

Depending on the presence of arm FP cavity, the functional forms of $\Phi(\Omega)$ and $\kappa(\Omega)$ can vary. t_{SR} and r_{SR} are SR mirror amplitude transmissivity and reflectivity respectively. And ϕ_{SR} is the phase detuning of the SR cavity. In general, if the readout is not at the phase quadrature but at a generic angle ζ, the strain calibrated noise spectral density derived from (2.37) is expressed as

$$
\begin{aligned}
S^h(\Omega) &= 2 \times \frac{(\cos\zeta \quad \sin\zeta)\,\boldsymbol{T}\,\langle 0|\begin{pmatrix}\hat{a}_1\\\hat{a}_2\end{pmatrix}(\hat{a}_1^\dagger \quad \hat{a}_2^\dagger)\,|0\rangle_{\text{sym}}\,\boldsymbol{T}^\dagger\begin{pmatrix}\cos\zeta\\\sin\zeta\end{pmatrix}}{(\cos\zeta \quad \sin\zeta)\,\bar{\boldsymbol{s}}(\Omega)\bar{\boldsymbol{s}}^\dagger(\Omega)\begin{pmatrix}\cos\zeta\\\sin\zeta\end{pmatrix}} \\[2mm]
&= \frac{(\cos\zeta \quad \sin\zeta)\,\boldsymbol{T}(\Omega)\boldsymbol{T}^\dagger(\Omega)\begin{pmatrix}\cos\zeta\\\sin\zeta\end{pmatrix}}{(\cos\zeta \quad \sin\zeta)\,\bar{\boldsymbol{s}}(\Omega)\bar{\boldsymbol{s}}^\dagger(\Omega)\begin{pmatrix}\cos\zeta\\\sin\zeta\end{pmatrix}}.
\end{aligned}
\tag{2.41}
$$

This equation should be regarded as after cancelling the Dirac delta $\delta(\Omega - \Omega')$ on both sides. The noise strain for GEO600 is plotted in Fig 4b.
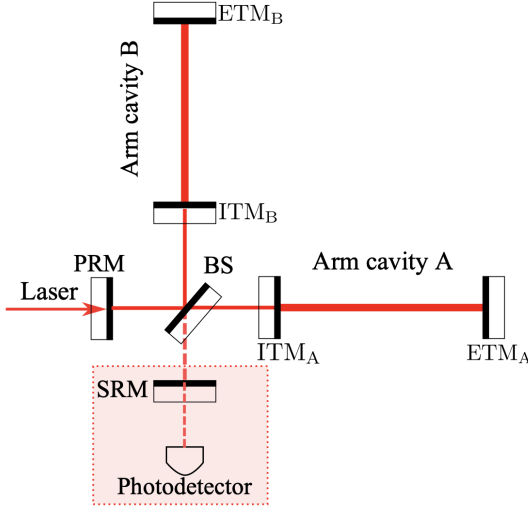
The idea of FDS to be introduced in the next section is simply to manipulate the vacuum entering the dark port. In terms of formalisms, a squeezed vacuum state $|\text{sqz}\rangle = \hat{S}(r, \phi)|0\rangle$ is used in the first line of (2.41). Or equivalently in the Heisenberg picture, the operators $\hat{a}_{1,2}$ undergo a squeeze transformation, while keeping the expectation value taken with respect to the original vacuum state $|0\rangle$.

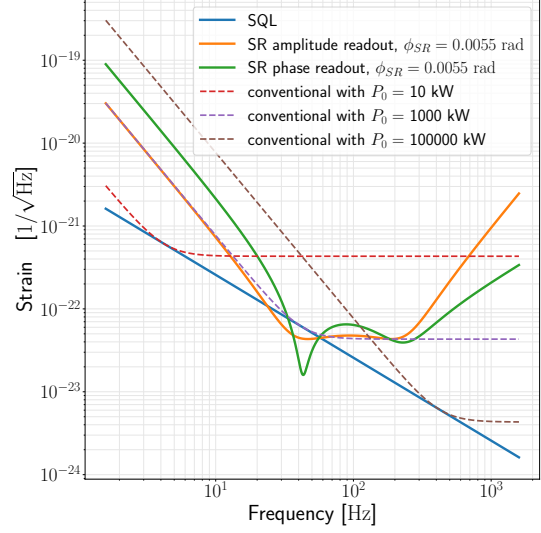# 3 Frequency dependent squeezing and optimization

3.1 Optimal squeezing for Resonant Sideband Extraction

The squeeze operator for a single sideband frequency Ω in two-photon formalism (in contrast to the form in the time domain (2.19)) is simply

$$\hat{S}(r, \phi) = \exp\left(re^{-2i\phi}\hat{a}_+\hat{a}_- - re^{2i\phi}\hat{a}_+^\dagger a_-^\dagger\right). \tag{3.1}$$

(a) The dual recycled interferometer

(b) Quantum noises in GEO600

Figure 4: The configuration of the a dual recycled interferometer and quantum noises. (a) is taken from [33]. ITM stands for internal test mass, which is fixed when GW passes by. PRM stands for power recycling mirror. And SRM stands for signal recycling mirror. (b) shows the quantum noise for GEO600 at the phase of the dual recycling interferometer from the left pannel, except that it is free of arm FP cavities. It is reproduced from the work of Harms *et al.* in [29]. For conventional interferometers the readout is always at phase quadrature.

With the help of rotation operators and matrices defined in Appendix A, the squeezed quadrature operators can be written as

$$
\begin{aligned}
\begin{pmatrix} \hat{a}'_1(\Omega) \\ \hat{a}'_2(\Omega) \end{pmatrix} &= \hat{S}^\dagger(r, \phi(\Omega)) \begin{pmatrix} \hat{a}_1(\Omega) \\ \hat{a}_2(\Omega) \end{pmatrix} \hat{S}(r, \phi(\Omega)) \\
&= \hat{R}^\dagger(\phi)\hat{S}^\dagger(r,0)\hat{R}^\dagger(-\phi) \begin{pmatrix} \hat{a}_1 \\ \hat{a}_2 \end{pmatrix} \hat{R}(-\phi)\hat{S}(r,0)\hat{R}(\phi) \\
&= \boldsymbol{R}(\phi)\boldsymbol{S}(r,0)\boldsymbol{R}(-\phi) \begin{pmatrix} \hat{a}_1 \\ \hat{a}_2 \end{pmatrix}
\end{aligned}
\tag{3.2}
$$

In practice only the rotation angle of the squeeze operator is made frequency dependent. Replace $\hat{a}_{1,2}$ by $\hat{a}'_{1,2}$ in (2.41), the noise strain for squeezed vacuum is expressed as

$$
S^h_{\text{SQZ}}(\Omega) = \frac{\begin{pmatrix} \cos\zeta & \sin\zeta \end{pmatrix} \boldsymbol{T}(\Omega)\boldsymbol{R}(\phi(\Omega)) \begin{pmatrix} e^{-2r} & 0 \\ 0 & e^{2r} \end{pmatrix} \boldsymbol{R}(-\phi(\Omega))\boldsymbol{T}^\dagger(\Omega) \begin{pmatrix} \cos\zeta \\ \sin\zeta \end{pmatrix}}{\begin{pmatrix} \cos\zeta & \sin\zeta \end{pmatrix} \bar{\boldsymbol{s}}(\Omega)\bar{\boldsymbol{s}}^\dagger(\Omega) \begin{pmatrix} \cos\zeta \\ \sin\zeta \end{pmatrix}}.
\tag{3.3}
$$

If the squeeze amplitude $r > 0$, it's better to choose amplitude readout $\zeta = 0$ and make

$$
\boldsymbol{R}(-\phi(\Omega))\boldsymbol{T}^\dagger(\Omega) \begin{pmatrix} \cos\zeta \\ \sin\zeta \end{pmatrix} \propto \begin{pmatrix} 1 \\ 0 \end{pmatrix}.
\tag{3.4}
$$

In the dual recycled interferometer, the matrix element of $\boldsymbol{T}$ is real up to a global phase factor, without which is denoted as T_{ij} below. This gives the theoretical optimal frequency

13

dependent squeezing angle

$$\phi(\Omega) = \frac{T_{12}(\Omega)\cos\zeta + T_{22}(\Omega)\sin\zeta}{T_{11}(\Omega)\cos\zeta + T_{21}(\Omega)\sin\zeta} \tag{3.5}$$

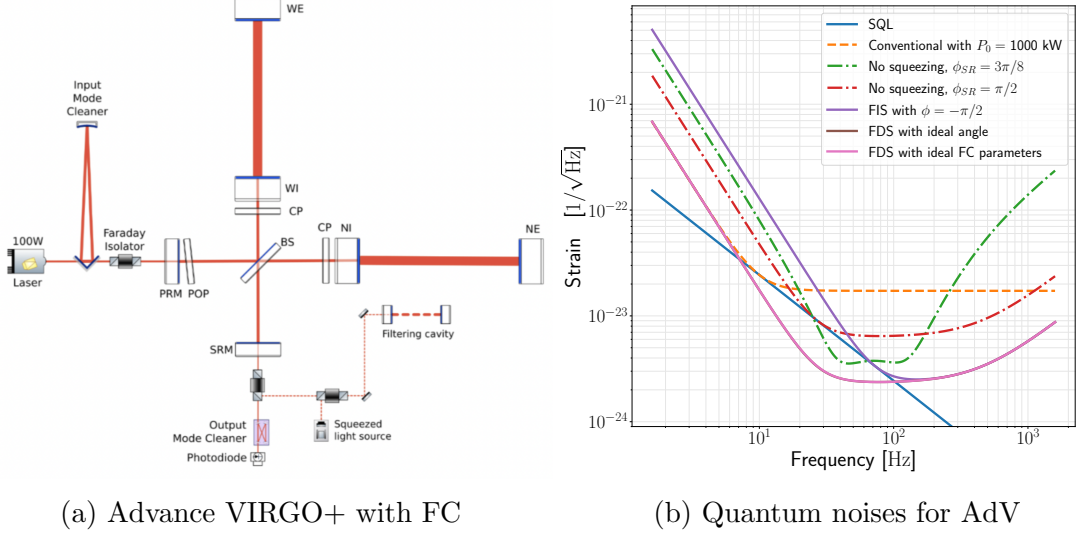(a) Advance VIRGO+ with FC   (b) Quantum noises for AdV

Figure 5: AdV+ configuration and the correponding quantum noises. (a) is taken from [22]. Compared to AdV, SR cavity is added and above all the filter cavity is installed to realise FDS. From (b), one can see that indeed setting the detuning SR phase ϕ_{SR} to $\pi/2$ realises a broad band configuration for the sensitivity curve, compared to $\phi_{\mathrm{SR}} = 3\pi/8$. For FIS both squeezing amplitude r and squeezing angle ϕ are constants. This only improves performance at high frequencies since the error ellipse basically doesn't get ponderomotively squeezed, in agreement with the intuitive picture from Fig 2b even the interferometer there is much simpler. The theoretical optimal FDS sensitivity curve plotted from (3.5) is invisible since it completely coincides with the curve produced with $\phi(\Omega)$ by $-\alpha_p(\Omega)$ with FC parameter chosen by (3.8).

The action of a generic squeeze operator simultaneously realises a pure squeezing and a rotation. But since the vacuum state is invariant under rotation, i.e., $\hat{R}(\phi)\,|0\rangle = |0\rangle$, if only the vacuum expectation and vacuum variance is computed, the effective action of a squeezing operator on the quadrature operators can be seen as

$$\hat{S}^{\dagger}(r,0)\hat{R}^{\dagger}(-\phi)\begin{pmatrix}\hat{a}_1\\\hat{a}_2\end{pmatrix}\hat{R}(-\phi)\hat{S}(r,0) = \boldsymbol{S}(r,0)\boldsymbol{R}(-\phi)\begin{pmatrix}\hat{a}_1\\\hat{a}_2\end{pmatrix}. \tag{3.6}$$

This means that in practice, the operation of a pure squeezing and rotation can be performed separately. The former is realised by Optical Parametric Oscillator, and the latter by Fabry-Pérot filter cavity (FC). The response of the quadrature operator going through an FC is derived in Appendix B

$$\begin{pmatrix}\hat{a}_{fc1}\\\hat{a}_{fc2}\end{pmatrix} = -e^{i\alpha_m}\begin{pmatrix}\cos\alpha_p & -\sin\alpha_p\\\sin\alpha_p & \cos\alpha_p\end{pmatrix}\begin{pmatrix}\hat{a}_1\\\hat{a}_2\end{pmatrix}, \qquad \alpha_p = \arctan\left(-\frac{2\gamma_{fc}\,\Delta\omega_{fc}}{\gamma_{fc}^2 - \Delta\omega_{fc}^2 + \Omega^2}\right). \tag{3.7}$$

For all practical purposes, one just has to match $\alpha_p(\Omega)$ with $-\phi(\Omega)$. This can be done with the help of machinary developed in [29, 35], i.e., choosing an intital squeezing angle, finding roots of characteristic equation etc. It turns out, in the RSE regime of advance detectors like LIGO and VIRGO, this matching is realised by setting both the detuning angular frequency $\Delta\omega_{fc}$ and FC bandwidth γ_{fc} to a certain value

$$\Delta\omega_{fc} = \gamma_{fc} = \frac{\Omega_{\mathrm{SQL}}}{\sqrt{2}} = \frac{1}{\sqrt{2}}\frac{t_{sr}}{1+r_{sr}}\frac{8}{c}\sqrt{\frac{P_{\mathrm{arm}}\omega_0}{mT_{\mathrm{arm}}}}, \tag{3.8}$$

where t_{sr} and r_{sr} are amplitude transmissivity and reflectivity of the SR mirror. P_{arm} is the circulating power in the arms and T_{arm} is the arm FP input mirror power transmissivity. This matching is shown in Fig 5b.

3.2 DRSE in VIRGO with one filter cavity

Although RSE can realise optimal squeezing with one FC, its marginal stability made it difficult to function as ideally as planned. The higher order modes(HOMs) of carrier laser generated inside the interferometer can leak out of SR cavity towards the photodiode. Therefore the current VIRGO detector is designed to function at detuned RSE (DRSE) regime to mitigate this problem, but with only one FC available so far for squeezing. In this case the DRSE detuning other than the $\pi/2$ already present in RSE is defined through $\phi_{\mathrm{SR}} = \frac{\pi}{2} + \Delta\phi_{\mathrm{DRSE}}$. Optimisation of the choice of $\Delta\phi_{\mathrm{DRSE}}$ and FC parameters are realised by numerical simulation using the Matlab code `gwinc` developed in the community, which computes the total noise budget instead of only the quantum noise discussed so far. It also takes into account of optical loss in current detector infrastucture. The performance of the detector is evaluated by the binary neutron star (BNS) range computed with a given signal-to-noise ratio of 8[20, 36]. From now on the carrier wavelength is set to 1064 nm.

The DRSE detuning satisfying $|\Delta\phi_{\mathrm{DRSE}}| \geq \frac{70\ \mathrm{nm}}{1064\ \mathrm{nm}} \cdot 2\pi$ is able to reduce HOMs by a factor of 10. To achieve a maximal BNS range without squeezing, the DRSE detuning length is set to 70 nm which gives a BNS range about 88 Mpc, an improvement of ~ 14 Mpc. The FC parameters, including FC detuning frequency $\Delta\omega_{fc}$, the initial squeezing angle ϕ_0 and the input mirror power transmissivity T_i which determines the bandwidth by $\gamma_{fc} = T_i f_{\mathrm{FSR}}/2$, are tuned to optimise BNS range by numerical calculation using `gwinc`. All the other parameters of the interferometer are fixed in accordance with current VIRGO design. The results are shown in Fig 6, Fig 7 and Fig 8.

4 Conclusion

In summary, the key concepts in quantum optics such as coherent and squeezed light are illustrated by the canonical quantisaton of a monochromatic light field. The formalism is generalised to a whole range of all possible continuous sideband frequencies, introducing the two-photon formalism. Then such notions are applied to a simple Michelson interferometer, which expalins most of the quantum physics for the light in the interferometer.

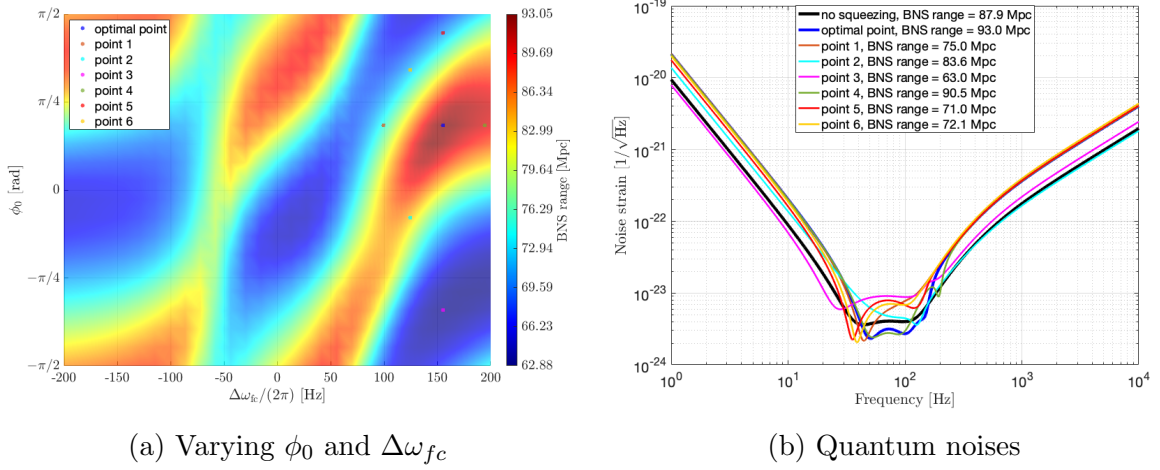(a) Varying ϕ_0 and $\Delta\omega_{fc}$

(b) Quantum noises

Figure 6: BNS range for varying the FC detuning frequency and corresponding quantum noises for a few points. On the left panel, the input FC mirror power transmissivity is set to $T_i = 5.62 \times 10^{-4} = 562\,\text{ppm}$ (ppm stands for "part per million"). The color bar represents BNS comoving range in unit of Mpc. The maximal BNS range is found to be roughly 93.0 Mpc, with an improvement of ~ 5 Mpc compared to the squeezing free case. Optimal pair of $\frac{\Delta\omega_{fc}}{2\pi}$ and ϕ_0 is found at $(153\,\text{Hz}, 29.4°)$. The strain of quantum noises for the optimal point and a few points are plotted with the same color as the points. This suggests that in the current DRSE regime, even if the squeezing with one FC diminishes sensitivity in the high and low frequency range, the BNS range improves. The typical frequency of GW generating by BNS roughly should roughly in the range of $(40,\ 110)$ Hz.

(a) Varying T_i and $\Delta\omega_{fc}$
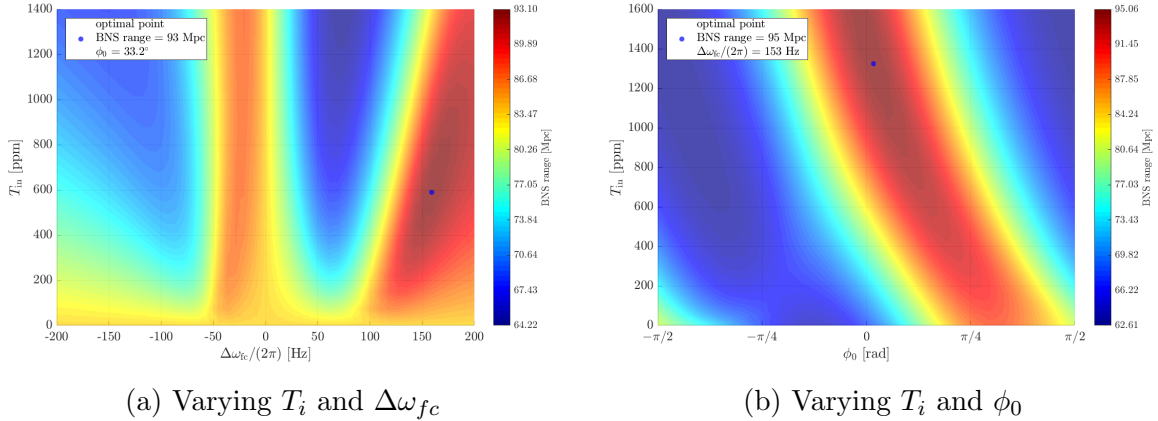
(b) Varying T_i and ϕ_0

Figure 7: BNS range for varying the other 2 pairs of FC parameters. On the left pannel the initial squeezing angle is fixed at $33.2°$. The optimal point is found at $(159\,\text{Hz}, 589\,\text{ppm})$, where the maximal BNS range is roughly the same as above. On the right pannel the FC detuning frequency is fixed at 153 Hz. The optimal point is found at $(3.1°, 1324\,\text{ppm})$, where the maximal BNS range exhibits an improvement of 2 Mpc compared to the previous case.

(a) Optimization over 3 FC parameters
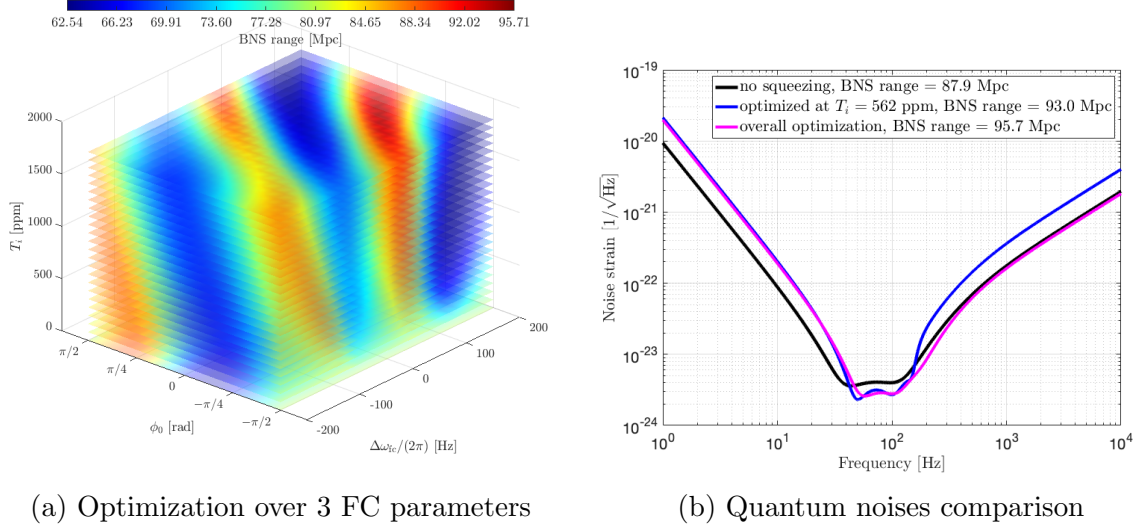
(b) Quantum noises comparison

Figure 8: Overall optimization over FC parameters and the corresponding quantum noises. The left pannel shows a 3D representation with the 3 FC parameters as axes and color representing BNS ranges. The optimal point lies at $(\Delta\omega_{\text{fc}}/(2\pi), \phi_0, T_i) = (133\,\text{Hz}, -14.2°, 1500\,\text{ppm})$, where the BNS range is maximized to be 95.7 Mpc. The faces of the cuboid roughly repeat the pattern of the pair optimization. The right pannel shows the comparison of quantum noises of optimal points in Fig 6b and the overall optimization. The overall optimization demonstrates a decrease of quantum noises at high frequencies compared to the $(\Delta\omega_{\text{fc}}, \phi_0)$ optimization, but the increase in BNS range is modest. This again implies that the GW frequency for typical BNS inspiral roughly lie in the range of (40, 120) Hz.

The input-output for the quadrature operators are derived. It is found that the vacuum fluctuation entering the bright port of the interferometer does not affect GW detection since the working point is locked at the dark fringe, in accordance with the physical intuition from the rotating phasor picture. The vacuum fluctuation entering from the dark port, on the other hand, does have the capability to introduce quantum noise to the signal at the readout photodiode, compromising the sensitivity of the GW detection. A crucial feature of this quantum noise is the ponderomotive squeezing and rotation described by Eq (2.34) and (2.35) and Fig 2b. This squeezing and rotation brought by the the interferometer response are to be counteracted by introducing the squeezed vacuum in a frequency dependent manner, in order to achieve a reduction of quantum noise over the whole frequency range.

In practice the FDS vacuum injected from the output port is realised by the action of squeezing and rotation separately by the use of optical parametric oscillator and filter cavity, thanks to the property of the invariance of the vacuum state of light field under rotation. It turns out that for the dual recycled interferometers, in the broad band regime, i.e., the case of RSE, an optimal choice of FC parameters allows to achieve the theoretical ideal FDS, as is shown by Eq (3.7) and Fig 5b. But given the current DRSE configuration of AdV+ due to the marginal stability of RSE and the leakage of higher order modes accompanied by it, numerical simulation of FDS is done to evaluate how well the detector functions with only one FC in the DRSE regime. The optimal SR detuning from RSE

is set to $\Delta\phi_{\mathrm{DRSE}} = \frac{70\,\mathrm{nm}}{1064\,\mathrm{nm}} \times 2\pi$ where 1064 nm is the carrier wavelength. For this the BNS range is computed by varying the the FC parameters, including the FC detuning frequency $\Delta\omega_{\mathrm{fc}}/(2\pi) = 153$ Hz, the initial squeezing angle ϕ_0 and the input FC mirror power transmissivity T_i which determines its bandwidth. Optimization over pairs of these three parameters shows that at current FC configuration with $T_i = 562$ ppm, the maximal BNS range is found at 93.0 Mpc, at $(\omega_{fc}/(2\pi), \phi_0) = 29.4°$. Simultaneous optimization over all three parameters shows a maximal BNS range of 95.7 Mpc at $\Delta\omega/(2\pi) = 133$ Hz, $\phi_0 = -14.2°$ and $T_i = 1500$ ppm. Compared to the squeezing free case giving a BNS range of 87.9 Mpc, the increase of BNS range is roughly 10%, giving an increase of about 30% of the accessible cosmological volume. This gives a qualitative assessment of the improvement of FDS in the current AdV+ configuration, demonstrating its advantage with respect to squeezing free AdV.

Not only will this optimisation strategy be instructive to the current GW detectors like AdV+, but it will also help assess the costs and gains of future detector configuration. For example, ET will be composed of 2 detectors, one optimized for the high signal frequency and the other for low signal frequency. The latter will be operated in DRSE configuration and need two FCs to further approach the optimal squeezing. The same kind of similational work can in principle be conducted. This will allow to evaluate the balance between the advantage of FDS by 2 FCs and the shortcomings of extra loss and squeeze degradation brought by another FC. The ultimate goal is to boost the sensitivity of GW detector to a new high level so that the accuracy of GW observation, the detection rate and the fathest probable distance can be augmented. Working towards this goal can bring impetus to the novel exciting field of multi-messenger astronomy, pushing forward our understanding of fundamental physics of gravitation, astrophysics and cosmology.

A   Calculation details and consistent sign convention for squeezing and rotation operators

This appendix provides calculation details for the action of squeezing and rotation on the quadrature operators. Although well documented in the literature, as far as is known by the author, the community does not have a common sign convention for the squeezing amplitude and the rotation angle. As a result, sign errors are not something uncommon in the published literature. The purpose of this appendix is to form a self-consistent sign for the convenience of theoretical investigation. The calculation is done for two-photon formalism, but for convenience the canonical quantisation for discrete frequency will be applied, i.e., the non-trivial canonical commutation relation is $[\hat{a}_\omega, \hat{a}_{\omega'}^\dagger] = \delta_{\omega\omega'}$.

The rotation and squeeze operator are defined respectively as[30, 31]

$$\hat{R}(\theta) \equiv \exp\left[i\theta(\hat{a}_+^\dagger \hat{a}_+ + \hat{a}_-^\dagger \hat{a}_-)\right], \tag{A.1}$$

$$\hat{S}(r, \phi) \equiv \exp\left(\chi^* \hat{a}_+ \hat{a}_- - \chi \hat{a}_+^\dagger \hat{a}_-^\dagger\right), \tag{A.2}$$

with $\chi = re^{2i\phi}$ and $\hat{a}_\pm = \hat{a}_{\omega_0 \pm \Omega}$ as in subsection 2.2. Notice that the sign of θ is different from [31], for a reason that will be clarified later. Before moving on to see their action

on the quadratures, a useful formula is worth mentioning. Suppose $\hat{A}$ and $\hat{B}$ are two operators (not neccessarily commute), for $x \in \mathbb{C}$ it can be proved that

$$f(x) = \exp\left(x\hat{A}\right)\hat{B}\exp\left(-x\hat{A}\right) = \hat{B} + \frac{x}{1!}[\hat{A}, \hat{B}] + \frac{x^2}{2!}\left[\hat{A}, [\hat{A}, \hat{B}]\right] + \cdots = \sum_{n=0}^{\infty} \frac{x^n}{n!}(\mathrm{ad}_{\hat{A}})^n\hat{B},$$

(A.3)

by Taylor expanding the operator valued function $f(x)$ and computing derivative to nth order $f^{(n)}(x)$. Recall the expression for the quadratures

$$\hat{a}_1 = \frac{1}{\sqrt{2}}(\hat{a}_+ + \hat{a}_-^\dagger) \qquad \hat{a}_2 = \frac{1}{\sqrt{2}i}(\hat{a}_+ - \hat{a}_-^\dagger).$$

(A.4)

Now when trying to compute $\hat{R}^\dagger(\theta)\hat{a}_1\hat{R}(\theta)$, we can write

$$\hat{R}^\dagger(\theta)\hat{a}_1\hat{R}(\theta) = \exp\left(\theta\hat{A}\right)\hat{a}_1\exp\left(-\theta\hat{A}\right), \qquad \text{with } \hat{A} = -i(\hat{a}_+^\dagger\hat{a}_+ + \hat{a}_-^\dagger\hat{a}_-).$$

(A.5)

Using the canonical commutation relation

$$\begin{aligned}
[\hat{A}, \hat{a}_1] &= -\frac{i}{\sqrt{2}}\left[\hat{a}_+^\dagger\hat{a}_+ + \hat{a}_-^\dagger\hat{a}_- , \ \hat{a}_+ + \hat{a}_-^\dagger\right] \\
&= -\frac{i}{\sqrt{2}}\left(\left[\hat{a}_+^\dagger\hat{a}_+ , \ \hat{a}_+\right] + \left[\hat{a}_-^\dagger\hat{a}_- , \ \hat{a}_-^\dagger\right]\right) \\
&= -\frac{1}{\sqrt{2}i}(\hat{a}_+ - \hat{a}_-) = -\hat{a}_2.
\end{aligned}$$

(A.6)

$$\begin{aligned}
[\hat{A}, -\hat{a}_2] &= \left[i(\hat{a}_+^\dagger\hat{a}_+ + \hat{a}_-^\dagger\hat{a}_-), \ \frac{1}{\sqrt{2}i}(\hat{a}_+ - \hat{a}_-^\dagger)\right] \\
&= \frac{1}{\sqrt{2}}\left(\left[\hat{a}_+^\dagger\hat{a}_+ , \ \hat{a}_+\right] - \left[\hat{a}_-^\dagger\hat{a}_- , \ \hat{a}_-^\dagger\right]\right) \\
&= \frac{1}{\sqrt{2}}(-\hat{a}_+ - \hat{a}_-^\dagger) = -\hat{a}_1.
\end{aligned}$$

(A.7)

This is enough to see the Taylor expansion of the rotated $\hat{a}_1$ using the formula (A.3),

$$\begin{aligned}
\hat{R}^\dagger(\theta)\hat{a}_1\hat{R}(\theta) &= \sum_{n=0}^{\infty}\frac{\theta^n}{n!}(\mathrm{ad}_{\hat{A}})^n\hat{a}_1 = \sum_{k=0}^{\infty}\frac{(-1)^k}{(2k)!}\theta^{2k}\hat{a}_1 - \sum_k\frac{(-1)^k}{(2k+1)!}\theta^{2k+1}\hat{a}_2 \\
&= \cos\theta\,\hat{a}_1 - \sin\theta\,\hat{a}_2.
\end{aligned}$$

(A.8)

The same calculation for $\hat{a}_2$ yields

$$\hat{R}^\dagger(\theta)\hat{a}_2\hat{R}(\theta) = \sin\theta\,\hat{a}_1 + \cos\theta\,\hat{a}_2.$$

(A.9)

Hence

$$\hat{R}^\dagger(\theta)\begin{pmatrix}\hat{a}_1 \\ \hat{a}_2\end{pmatrix}\hat{R}(\theta) = \boldsymbol{R}(\theta)\begin{pmatrix}\hat{a}_1 \\ \hat{a}_2\end{pmatrix} = \begin{pmatrix}\cos\theta & -\sin\theta \\ \sin\theta & \cos\theta\end{pmatrix}\begin{pmatrix}\hat{a}_1 \\ \hat{a}_2\end{pmatrix}.$$

(A.10)

The rotation matrix appearing here is the one taking the *active* viewpoint, i.e, it gives the new coordinate of the rotated points in the old basis. A difference of the sign of θ

correspond to the difference of active and passive viewpoint. However, the active viewpoint better aligns with physical intuition because Heisenberg picture is used throughout the main text. When talking about the squeezed or rotated vacuum the transformation is considered as acting on the observables, while vacuum state is still used to take expectation values. It's the vacuum that gets rotated and squeezed, not the readout device, meaning we are measuring the *new* observables in the *old* basis. Hence the active viewpoint is more appropriate for theoretical analysis.

One can proceed with the squeezing operator. For $\hat{a}_1$,

$$\hat{S}^\dagger(r,\phi)\hat{a}_1\hat{S}(r,\phi) = \exp\left(\hat{A}\right)\hat{a}_1\exp\left(-\hat{A}\right) = \sum_{n=0}^{\infty}\frac{1}{n!}(\mathrm{ad}_{\hat{A}})^n\hat{a}_1, \quad \hat{A} = \chi\hat{a}_+^\dagger\hat{a}_-^\dagger - \chi^*\hat{a}_+\hat{a}_-.$$
(A.11)

$$\mathrm{ad}_{\hat{A}}\hat{a}_1 = -\frac{\chi}{\sqrt{2}}\hat{a}_-^\dagger - \frac{\chi^*}{\sqrt{2}}\hat{a}_+ \equiv \hat{B}.$$
(A.12)

$$(\mathrm{ad}_{\hat{A}})^2\hat{a}_1 = [\hat{A},\,\hat{B}] = |\chi|^2\hat{a}_1 = r^2\hat{a}_1.$$
(A.13)

From here it can be deduced that

$$\hat{S}^\dagger(r,\phi)\hat{a}_1\hat{S}(r,\phi) = \sum_{k=0}^{\infty}\frac{r^{2k}}{(2k)!}\hat{a}_1 + \sum_{k=0}^{\infty}\frac{r^{2k}}{(2k+1)!}\left(-\frac{re^{2i\phi}}{\sqrt{2}}\hat{a}_-^\dagger - \frac{re^{-2i\phi}}{\sqrt{2}}\hat{a}_+\right)$$
(A.14)
$$= \cosh r\,\hat{a}_1 - \cos 2\phi\sinh r\,\hat{a}_1 - \sin 2\phi\sinh r\,\hat{a}_2.$$

Together with the same steps of calculation for $\hat{a}_2$, the squeezed quadrature can be written as

$$\hat{S}^\dagger(r,\phi)\begin{pmatrix}\hat{a}_1\\\hat{a}_2\end{pmatrix}\hat{S}(r,\phi) = \begin{pmatrix}\cosh r - \cos 2\phi\sinh r & -\sin 2\phi\sinh r\\ -\sin 2\phi\sinh r & \cosh r + \cos 2\phi\sinh r\end{pmatrix}\begin{pmatrix}\hat{a}_1\\\hat{a}_2\end{pmatrix}$$
$$= \boldsymbol{S}(r,\phi)\begin{pmatrix}\hat{a}_1\\\hat{a}_2\end{pmatrix}.$$
(A.15)

This coincides with the result of (2.10) for the monochromatic light, first derived by Caves in [27]. The form of squeezing matrix $\boldsymbol{S}(r,\phi)$ implies, making use of (A.10)

$$\boldsymbol{S}(r,\phi)\begin{pmatrix}\hat{a}_1\\\hat{a}_2\end{pmatrix} = \begin{pmatrix}\cos\phi & -\sin\phi\\\sin\phi & \cos\phi\end{pmatrix}\begin{pmatrix}e^{-r} & 0\\0 & e^r\end{pmatrix}\begin{pmatrix}\cos\phi & \sin\phi\\-\sin\phi & \cos\phi\end{pmatrix}\begin{pmatrix}\hat{a}_1\\\hat{a}_2\end{pmatrix}$$
$$= \boldsymbol{R}(\phi)\boldsymbol{S}(r,0)\boldsymbol{R}(-\phi)\begin{pmatrix}\hat{a}_1\\\hat{a}_2\end{pmatrix}$$
(A.16)
$$= \left[\hat{R}(-\phi)\hat{S}(r,0)\hat{R}(\phi)\right]^\dagger\begin{pmatrix}\hat{a}_1\\\hat{a}_2\end{pmatrix}\left[\hat{R}(-\phi)\hat{S}(r,0)\hat{R}(\phi)\right].$$

This suggests that for a generic squeezing operator $\hat{S}(r,\phi)$ with squeezing amplitude r and rotation angle ϕ,

$$\hat{S}(r,\phi) = \hat{R}^\dagger(\phi)\hat{S}(r,0)\hat{R}(\phi),$$
(A.17)

i.e., it is obtained by rotating the pure squeezing operator $\hat{S}(r,0)$ by an angle of ϕ. This is also Eq (3.16) in [31], but the authors derived it with the wrong sign of rotation angle. Their definition of the rotation operator corresponds to the passive viewpoint of rotation, which is in conflict with the Heisenberg picture.

B Transfer matrix of the filter cavity

To derive the response of the filter cavity (FC) for the input and output mode, the easiest way is to start from monochromatic light. Consider a quantum light field with single angular frequency ω, an FC with cavity length l, input mirror amplitude transmissivity and reflectivity t and r, whose inner faces will induce a phase shift of π for the light upon reflection, like the figure below.
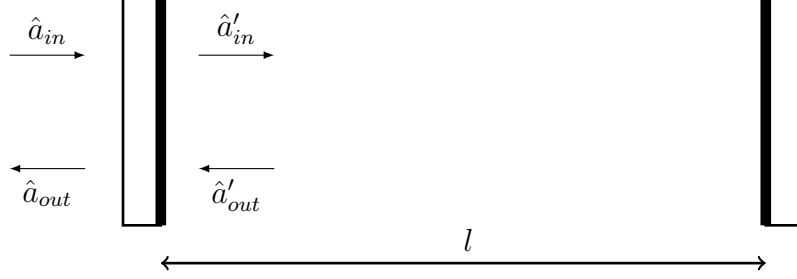

Figure 9: Modes in the filter cavity.

It suffices to consider only the annihilation operator as in (2.2), ignoring the field strength constant, the spatial dependence and the negative frequency part. Then one has the linear relations

$$\hat{a}'_{in} = t\hat{a}_{in} - r\hat{a}'_{out}, \tag{B.1a}$$

$$\hat{a}_{out} = r\hat{a}_{in} + t\hat{a}'_{out}, \tag{B.1b}$$

$$\hat{a}'_{out} = -e^{2ikl}\hat{a}'_{in}. \tag{B.1c}$$

Say the frequency ω is the upper sideband frequency $\omega_0 + \Omega$, the phase $\varphi = 2kL$, defined up to modulo 2π can be written as

$$\varphi = 2\frac{\omega}{c}l = 2\frac{\omega_0 + \Omega}{c}l = \frac{\omega_0 + \Omega}{c/(2l)} = \frac{\Omega - (2\pi N f_{\text{FSR}} - \omega_0)}{f_{\text{FSR}}} = \frac{\Omega - \Delta\omega_{fc}}{f_{\text{FSR}}}, \tag{B.2}$$

where $f_{\text{FSR}} \equiv c/(2l)$ is the free spectral range, the smallest frequency in resonant with the cavity, and $N \in \mathbb{N}$ such that $\Omega < 2\pi f_{\text{FSR}}$. $2\pi N f_{\text{FSR}} - \omega_0$ is the detuning angular frequency of FC with respect to the carrier. From the linear relations (B.1),

$$\hat{a}_{out} = \left(r - \frac{t^2 e^{i\varphi}}{1 - re^{i\varphi}}\right)\hat{a}_{in} \equiv r_{fc}\hat{a}_{in}. \tag{B.3}$$

In practice, the FC used in experiments satisfied $\varphi \lesssim 10^{-2}$, and the input mirror transmissivity is also small. Applying Taylor expansion to first order

$$e^{i\varphi} \approx 1 + i\varphi \qquad r = \sqrt{1 - t^2} \approx 1 - \frac{1}{2}t^2, \tag{B.4}$$

the reflectivity of the whole FC for the upper sideband can be approximated as

$$r_{fc} \approx -\frac{1 + i\xi}{1 - i\xi} = -e^{i\alpha_{fc}}, \tag{B.5}$$

where $\xi = 2\varphi/t^2$, and $\alpha_{fc} = 2\arctan \xi$.

To extend the result to two-photon formalism, just notice

$$\begin{pmatrix} \hat{b}_1 \\ \hat{b}_2 \end{pmatrix} = A \begin{pmatrix} \hat{b}_{\omega_0+\Omega} \\ \hat{b}^\dagger_{\omega_0-\Omega} \end{pmatrix} = A T_{fc} \begin{pmatrix} \hat{a}_+ \\ \hat{a}^\dagger_- \end{pmatrix}, \qquad \text{(B.6)}$$

where for simplicity $\hat{a}$ stands for input mode and $\hat{b}$ for output mode, and

$$A = \begin{pmatrix} \frac{1}{\sqrt{2}} & \frac{1}{\sqrt{2}} \\ \frac{1}{\sqrt{2}i} & -\frac{1}{\sqrt{2}i} \end{pmatrix}, \qquad T_{fc} = \begin{pmatrix} r_{fc+} & 0 \\ 0 & r^*_{fc-} \end{pmatrix}. \qquad \text{(B.7)}$$

Hence, the input-output relation of FC for the quadratures is computed as

$$\begin{aligned} \begin{pmatrix} \hat{b}_1 \\ \hat{b}_2 \end{pmatrix} &= A\, T_{fc}\, A^{-1} \begin{pmatrix} \hat{a}_1 \\ \hat{a}_2 \end{pmatrix} \\ &= \begin{pmatrix} \frac{1}{\sqrt{2}} & \frac{1}{\sqrt{2}} \\ \frac{1}{\sqrt{2}i} & -\frac{1}{\sqrt{2}i} \end{pmatrix} \begin{pmatrix} r_{fc+} & 0 \\ 0 & r^*_{fc-} \end{pmatrix} \begin{pmatrix} \frac{1}{\sqrt{2}} & -\frac{1}{\sqrt{2}i} \\ \frac{1}{\sqrt{2}} & \frac{1}{\sqrt{2}i} \end{pmatrix} \begin{pmatrix} \hat{a}_1 \\ \hat{a}_2 \end{pmatrix} \\ &= -e^{i\alpha_m} \begin{pmatrix} \cos\alpha_p & -\sin\alpha_p \\ \sin\alpha_p & \cos\alpha_p \end{pmatrix} \begin{pmatrix} \hat{a}_1 \\ \hat{a}_2 \end{pmatrix}, \end{aligned} \qquad \text{(B.8)}$$

where

$$\alpha_m = \frac{\alpha_{fc+} - \alpha_{fc-}}{2}, \quad \alpha_p = \frac{\alpha_{fc+} + \alpha_{fc-}}{2}, \quad \alpha_{fc\pm} = 2\arctan\left[\frac{2}{t^2 f_{\mathrm{FSR}}}(\pm\Omega - \Delta\omega_{fc})\right]. \qquad \text{(B.9)}$$

Finally (B.8) can be further written as

$$\begin{pmatrix} \hat{b}_1 \\ \hat{b}_2 \end{pmatrix} = -e^{i\alpha_m} \boldsymbol{R}(\alpha_p) \begin{pmatrix} \hat{a}_1 \\ \hat{a}_2 \end{pmatrix}, \qquad \alpha_p = -\arctan\left(\frac{2\Delta\omega_{fc}\gamma_{fc}}{\gamma_{fc}^2 + \Omega^2 - \Delta\omega_{fc}^2}\right), \qquad \text{(B.10)}$$

where $\gamma_{fc} = t^2 f_{\mathrm{FSR}}/2$ is the bandwidth of FC. This is just Eq (3.7) in the main text. The overall phase factor $-e^{i\alpha_m}$ does not have any effect on the noise spectral density.

References

[1] Albert Einstein. Näherungsweise Integration der Feldgleichungen der Gravitation. *Sitzungsberichte der Königlich Preussischen Akademie der Wissenschaften*, pages 688–696, January 1916.

[2] Albert Einstein. Über Gravitationswellen. *Sitzungsberichte der Königlich Preussischen Akademie der Wissenschaften*, pages 154–167, January 1918.

[3] Felix A E Pirani. Republication of: On the physical significance of the riemann tensor. *General Relativity and Gravitation*, 41(5):1215–1232, May 2009.

[4] Cécile Morette Dewitt and Dean Rickles. The role of gravitation in physics : report from the 1957 chapel hill conference. 2011.

[5] R.A. Hulse and J.H. Taylor. Discovery of a pulsar in a binary system. *Astrophys. J. Lett.*, 195:L51–L53, 1975.

[6] J. Weber. Detection and generation of gravitational waves. *Phys. Rev.*, 117:306–313, Jan 1960.

[7] Robert L. Forward. Wideband laser-interferometer graviational-radiation experiment. *Phys. Rev. D*, 17:379–390, Jan 1978.

[8] G. E. Moss, L. R. Miller, and R. L. Forward. Photon-noise-limited laser transducer for gravitational antenna. *Appl. Opt.*, 10(11):2495–2498, Nov 1971.

[9] T. Accadia *et al.* Virgo: a laser interferometer to detect gravitational waves. *Journal of Instrumentation*, 7(03):P03012, mar 2012.

[10] Alex Abramovici, William E. Althouse, Ronald W. P. Drever, Yekta Gürsel, Seiji Kawamura, Frederick J. Raab, David Shoemaker, Lisa Sievers, Robert E. Spero, Kip S. Thorne, Rochus E. Vogt, Rainer Weiss, Stanley E. Whitcomb, and Michael E. Zucker. Ligo: The laser interferometer gravitational-wave observatory. *Science*, 256(5055):325–333, 1992.

[11] B. P. Abbott *et.al.* Observation of gravitational waves from a binary black hole merger. *Phys. Rev. Lett.*, 116:061102, Feb 2016.

[12] Jorge L. Cervantes-Cota, Salvador Galindo-Uribarri, and George F. Smoot. A brief history of gravitational waves. *Universe*, 2(3), 2016.

[13] The LIGO Scientific Collaboration, the Virgo Collaboration, and the KAGRA Collaboration. Gwtc-3: Compact binary coalescences observed by ligo and virgo during the second part of the third observing run, 2021.

[14] B. P. Abbott *et al.* Gw170817: Observation of gravitational waves from a binary neutron star inspiral. *Phys. Rev. Lett.*, 119:161101, Oct 2017.

[15] T. Baker, E. Bellini, P. G. Ferreira, M. Lagos, J. Noller, and I. Sawicki. Strong constraints on cosmological gravity from gw170817 and grb 170817a. *Phys. Rev. Lett.*, 119:251301, Dec 2017.

[16] B. P. Abbott *et al.* A gravitational-wave standard siren measurement of the hubble constant. *Nature*, 551(7678):85–88, November 2017.

[17] A. Palmese, C. R. Bom, S. Mucesh, and W. G. Hartley. A standard siren measurement of the hubble constant using gravitational-wave events from the first three ligo/virgo observing runs and the desi legacy survey. *The Astrophysical Journal*, 943(1):56, jan 2023.

[18] B. P. Abbott *et al.* Gw170817: Measurements of neutron star radii and equation of state. *Phys. Rev. Lett.*, 121:161101, Oct 2018.

[19] F Acernese *et al.* Status of virgo. *Classical and Quantum Gravity*, 25(11):114045, may 2008.

[20] Lee Samuel Finn and David F. Chernoff. Observing binary inspiral in gravitational radiation: One interferometer. *Phys. Rev. D*, 47:2198–2219, Mar 1993.

[21] F Acernese *et al*. Advanced virgo: a second-generation interferometric gravitational wave detector. *Classical and Quantum Gravity*, 32(2):024001, dec 2014.

[22] Raffaele Flaminio. Status and plans of the Virgo gravitational wave detector. In *SPIE Astronomical Telescopes + Instrumentation 2020*, volume 11445, page 1144511, Online, United States, December 2020.

[23] Carlton M. Caves. Quantum-mechanical radiation-pressure fluctuations in an interferometer. *Phys. Rev. Lett.*, 45:75–79, Jul 1980.

[24] V. B. Braginskiĭ. Classical and Quantum Restrictions on the Detection of Weak Disturbances of a Macroscopic Oscillator. *Soviet Journal of Experimental and Theoretical Physics*, 26:831, April 1968.

[25] Carlton M. Caves, Kip S. Thorne, Ronald W. P. Drever, Vernon D. Sandberg, and Mark Zimmermann. On the measurement of a weak classical force coupled to a quantum-mechanical oscillator. i. issues of principle. *Rev. Mod. Phys.*, 52:341–392, Apr 1980.

[26] Alessandra Buonanno and Yanbei Chen. Quantum noise in second generation, signal-recycled laser interferometric gravitational-wave detectors. *Phys. Rev. D*, 64:042006, Jul 2001.

[27] Carlton M. Caves. Quantum-mechanical noise in an interferometer. *Phys. Rev. D*, 23:1693–1708, Apr 1981.

[28] H. J. Kimble, Yuri Levin, Andrey B. Matsko, Kip S. Thorne, and Sergey P. Vyatchanin. Conversion of conventional gravitational-wave interferometers into quantum nondemolition interferometers by modifying their input and/or output optics. *Phys. Rev. D*, 65:022002, Dec 2001.

[29] Jan Harms, Yanbei Chen, Simon Chelkowski, Alexander Franzen, Henning Vahlbruch, Karsten Danzmann, and Roman Schnabel. Squeezed-input, optical-spring, signal-recycled gravitational-wave detectors. *Phys. Rev. D*, 68:042001, Aug 2003.

[30] Carlton M. Caves and Bonny L. Schumaker. New formalism for two-photon quantum optics. i. quadrature phases and squeezed states. *Phys. Rev. A*, 31:3068–3092, May 1985.

[31] Bonny L. Schumaker and Carlton M. Caves. New formalism for two-photon quantum optics. ii. mathematical foundation and compact notation. *Phys. Rev. A*, 31:3093–3111, May 1985.

[32] Simon Chelkowski. *Squeezed Light and Laser Interferometric Gravitational Wave Detectors*. PhD thesis, Hannover U., 2007.

[33] Haixing Miao. *Exploring macroscopic quantum mechanics in optomechanical devices.* PhD thesis, 2010.

[34] M. Maggiore. *Gravitational Waves: Volume 1: Theory and Experiments.* Gravitational Waves. OUP Oxford, 2008.

[35] Patricia Purdue and Yanbei Chen. Practical speed meter designs for quantum nondemolition gravitational-wave interferometers. *Phys. Rev. D*, 66:122004, Dec 2002.

[36] Hsin-Yu Chen, Daniel E Holz, John Miller, Matthew Evans, Salvatore Vitale, and Jolien Creighton. Distance measures in gravitational-wave astrophysics and cosmology. *Classical and Quantum Gravity*, 38(5):055010, jan 2021.